Growth of randomly oriented single-crystalline tin (IV) oxide nanobelts: Control on the predominant crystalline growth axis

Samad Bazargan and K. T. Leung[a)]
WATLab and Department of Chemistry, University of Waterloo, Waterloo, Ontario N2L 3G1, Canada

(Received 26 October 2012; accepted 22 February 2013; published online 14 March 2013)

One-dimensional nanobelts of tin (IV) oxide are synthesized by using a newly introduced catalyst-assisted pulsed laser deposition method along two growth directions of [010] and [101]. An *ex situ* mask-induced growth gradient technique is employed to investigate the growth evolution of the nanobelts on oxidized-Si, H-terminated Si, and Al_2O_3(0001) substrates by helium ion microscopy, which reveals four stages of growth including catalyst detachment, horizontal nanorod growth, deflection, and the final nanobelt growth. X-ray diffraction and transmission electron microscopy studies show that in spite of the deflections and changes in the growth direction, the nanobelts have, remarkably, maintained their single-crystalline structure throughout the growth by only changing their crystalline growth axis. This has enabled us to influence the preferred growth axis by establishing a crystalline relation between the nanobelts and an appropriate substrate that pins the nanobelts in the initial growth stage. This growth control provides an important means to selectively promote growth of the predominant side planes of the nanobelts, which can then be separated for appropriate applications based on the different growth kinetics of [010] and [101] growth direction. © *2013 American Institute of Physics*. [http://dx.doi.org/10.1063/1.4794741]

I. INTRODUCTION

One-dimensional (1D) nanostructures of transparent conducting oxides (TCO) have received a lot of recent attention due to their high surface-to-volume ratios and unique optical,[1] electronic and optoelectronic,[2,3] mechanical,[4] electromechanical,[5] and chemical properties.[6] Tin (IV) oxide is one of these interesting TCO materials with a particularly high chemical and thermal stability,[7] and a prominent sensitivity towards reducing gases.[8] Numerous methods have been developed to synthesize 1D SnO_2 nanostructures, which can potentially be used as high-performance gas sensors,[6] chemical sensors,[9] and optical waveguides,[1] and as promising electron field emitters[10] and nanoelectronic components.[2] These synthesis methods include plasma-enhanced chemical vapor deposition,[11] sol-gel,[12] solution-phase chemistry,[13] laser ablation,[3,14] and spray pyrolysis,[15] with thermal evaporation[16] being the most widely used method. Pulsed laser deposition (PLD), which is one of the primary methods for thin-film deposition of oxides, has been largely overlooked, and there are only a rather limited number of PLD applications for 1D nanostructure growth of oxides.[17–19] Epitaxial growth, ease of doping, and multiple target deposition are some of the unique advantages of the PLD method, which can lead to great control in the alignment, growth axis control, and homo- and hetero-structure synthesis of 1D nanostructures.

We have recently reported the catalyst-assisted PLD (C-PLD) synthesis of 1D SnO_2 nanostructures by prefabricating a uniform layer of gold nanoislands (GNIs) on an oxidized Si substrate.[20] In particular, SnO_2 nanobelts were obtained through a vapour–liquid–solid (VLS) mechanism at 400 mTorr Ar with a relatively low substrate temperature of 500 °C. The aforementioned conditions have led to the growth of SnO_2 nanobelts with two different growth axes of [101] and [100] each with their own different narrow/wide side surface planes of (101)/(010) and (101)/2.7° miscut (201), respectively. This is in contrast to the earlier 1D tetragonal SnO_2 nanostructure growth studies, where only a single growth axis is reported.[3,14,21] Of special interest is the observed miscut (201) surface plane, which is expected to exhibit higher surface conductivity and reactivity due to the high defect density on its stepped surface, and has not been reported in earlier studies.

Studying the growth evolution of the SnO_2 nanobelts can allow us to develop further control on their growth parameters, including the nucleation sites, the growth alignment with respect to the substrate, and the crystalline growth axis and consequently their side-surface planes. In earlier studies, Wu *et al.*[22] and Schmidt *et al.*[23] reported the growth evolution of Si nanowires promoted by Au catalysts through the VLS mechanism on Si substrates. However, to date, the growth evolution of 1D SnO_2 nanostructures promoted by catalysts, especially on substrates without any epitaxial relation to SnO_2, remains unknown. This difficulty is due to the random orientation of the as-grown 1D SnO_2 nanostructures on generally amorphous and/or insulating substrates.[3,14,16,21] In the present work, as one of the advantages of the PLD method, we use a mask-induced growth gradient technique to investigate the growth evolution of the nanobelts deposited by the catalyst-assisted PLD method on GNI/substrate templates with or without epitaxial relation to SnO_2. Various stages of growth including catalyst detachment, horizontal nanorod growth, deflection, and the final nanobelt growth

a)E-mail: tong@uwaterloo.ca.

are identified. It is found that the changes and deflections in growth direction do not alter the single-crystalline nature of the nanobelts and occur only by switching the growth orientation to a different plane without disturbing the crystalline structure of these nanostructures. Therefore, in spite of their random orientation on the substrate, their growth axes can be manipulated by pinning the nanobelts to the appropriate substrate, which has been demonstrated for promoting growth in the [100] direction. This study provides new insight into how the VLS growth mechanism drives the synthesis of SnO_2 nanobelts on three different templates, which reveals the possible control on the predominated crystalline growth orientation of these seemingly random 1D nanostructures.

II. EXPERIMENTAL DETAILS

A KrF excimer laser (248 nm wavelength), operating with a laser fluence of 350 mJ/pulse and a repetition rate of 5 Hz, is used for ablating a SnO_2 target in a high vacuum chamber with a base pressure of 8×10^{-8} torr. The target is prepared by cold-pressing SnO_2 powders (Aldrich, 99.90% purity) at a pressure of 20 MPa followed by sintering at 900 °C in air for 24 h. The resulting dense target is necessary in order to maintain its integrity to withstand the impact of the laser pulse (with a high energy density) for ablation over an extended period of time. Depositions are carried out on gold nanoisland templates supported on two different substrates for 90 min in 400 mTorr of Ar at a flow rate of 20 sccm. Single-side polished Si(100) substrates (10×10 mm^2) are chemically oxidized (ox-Si) using H_2O_2 and NH_4OH solutions according to a RCA cleaning procedure,[24] while polished Al_2O_3(0001) substrates (5×5 mm^2) are used as purchased. To produce the GNI template, we sputter a thin (<10 nm) layer of Au on the substrates followed by thermal annealing (generally from 500 °C to 700 °C) for 1 h. The average size of the GNIs can be controlled by the thickness of the gold layer and the annealing temperature as described in detail in Ref. 25. The target-to-substrate distance is kept at 50 mm, where the substrate is in close proximity to the top of the visible region of the plume, and the substrate temperature is maintained at 500 °C by radiative heating of infrared lamps from the backside for the duration of the deposition.

A Zeiss Orion Plus helium ion microscope (HIM) and a LEO FESEM 1530 scanning electron microscope (SEM) equipped with secondary electron and back-scattered electron detectors are used to examine the morphology of the resulting SnO_2 nanostructures. The HIM used for our studies is equipped with a secondary electron detector and a back-scattered ion detector, and a flood gun to facilitate imaging of insulating samples (such as Al_2O_3). The HIM is especially suitable for the growth studies due to its larger depth-of-field compared to SEM. The corresponding crystal structure is studied by using a PANalytical MRD X'pert Pro diffractometer with a Cu Kα source. X-ray diffraction (XRD) studies are performed using a parallel X-ray beam setup with an X-ray mirror in the incident beam side and a parallel plate collimator (with a plate spacing of 0.27°) in the diffracted beam side. The symmetrical ω-2θ scans are performed using the Bragg-Brentano geometry with this setup, while the glancing-incidence XRD (GIXRD) experiments are conducted with a fixed incidence angle of $\omega = 0.3°$ over the desirable 2θ range. The crystalline structure and growth direction of selected SnO_2 nanobelt sections are studied by a JEOL 2010F transmission electron microscope (TEM) operated at 200 kV. For these measurements, samples were scraped off the substrate using a blade, mixed with high-performance liquid chromatography grade methanol in a beaker and sonicated for 10 min, and the resulting suspension was then transferred onto a holey carbon copper grid.

III. RESULTS AND DISCUSSION

A. SEM and HIM studies of growth morphology

In the catalyst-assisted PLD method, growth evolution can be studied by creating a growth gradient on the substrate with a mask placed in between the laser plume and the substrate. The substrate is mounted perpendicular to the plume expansion direction on a windowed substrate holder, which serves as a mask covering 2 mm of the perimeter of the substrate. Examining the as-grown nanostructures across this masked area reveals information about the growth progress of the nanostructures as a result of different exposures to the ablated material across the masked area. The observed growth advancement of nanostructures using this technique is also consistent with our results obtained in separate experiments by varying the deposition time. Figure 1 shows the different stages of growth using the mask-induced growth gradient technique for the nanobelts PLD-grown at 500 °C in 400 mTorr of Ar on a GNI/ox-Si template. The GNIs formed on the ox-Si (Figure 1(a)) exhibit a generally dome-shaped morphology with an average diameter of 50 nm and a near-Gaussian size distribution. In spite of the possible Au silicide formation[25] in the GNI/ox-Si interface, the GNIs are found to be readily dislodged during the deposition at 500 °C. This is in marked contrast to the GNI/H–Si template where GNIs are strongly bound, possibly due to a larger number of Si sites available for Au silicide formation. Figure 1(b) shows preferential growth of SnO_2 nanostructures almost exclusively at the GNI sites instead of the bare ox-Si areas (not covered by GNIs). In particular, the growth of a SnO_2 nanostructure pushes up and detaches the GNI, tilting the sharp Au–SnO_2 interface (e.g., those marked by arrows in Figure 1(b)) and giving rise to a wedge-shaped SnO_2 stub. The observed growth evolution is indicative of a typical VLS growth mechanism,[26] in which most of the vapour undergoes dissolution in the GNIs preferentially instead of adsorption on the bare ox-Si surface, consistent with a higher material absorption rate on GNI near its melting point. The dissolved vapour subsequently precipitates to form the SnO_2 nanostructure at the Au and Si interface, leading to the detachment of the GNI. As deposition continues, the faceted SnO_2 stubs grow horizontally in length, filling up the open areas in between the GNIs. The Au–SnO_2 interfaces of the resulting nanorods remain sharp and become more vertical (Figure 1(c), with arrows marking the interfaces). As the nanostructure growth continues, these horizontal

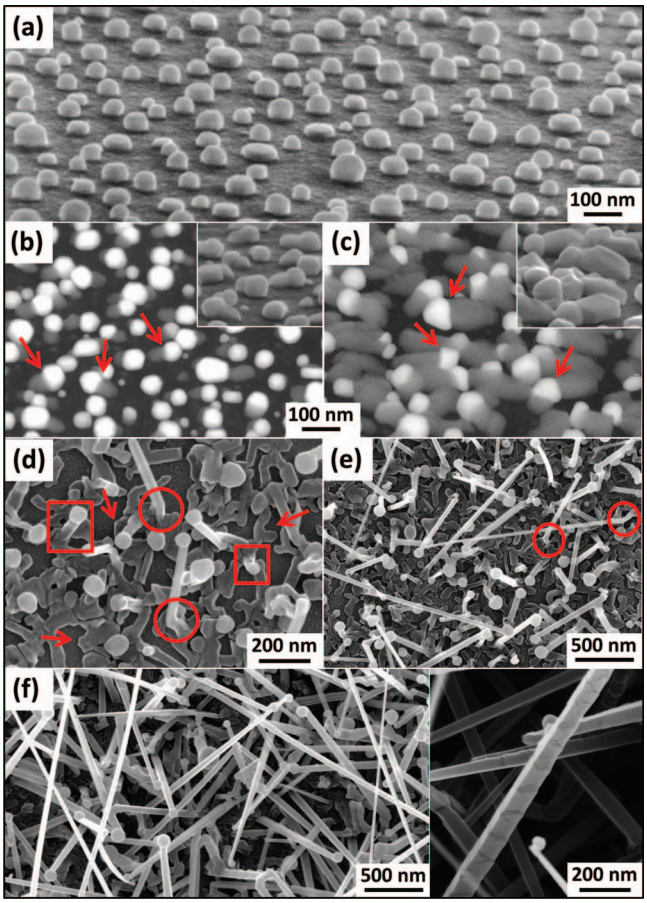

FIG. 1. Secondary-electron SEM image collected at 70° tilt of (a) a gold nanoisland/oxidized-Si template, and backscattered-electron SEM images of the corresponding Au/SnO_2 nanostructures at (b) the growth initiation and (c) nanorod growth stages (insets show secondary-electron SEM images) with arrows marking the interfaces between Au (brighter objects) and SnO_2 nanostructures (darker objects). HIM images of (d) nanorods in the deflection stage, and of nanobelts (e) in their initial and (f) final stages of growth, in 400 mTorr Ar at 500 °C. The arrows, open squares, and open circles in (d) and (e) mark the horizontal deflections, vertical deflections, and kinks, respectively. The inset in (f) shows the rectangular cross section of a typical nanobelt.

nanostructures start to run into one another and cause abrupt changes in their growth directions (e.g., marked by arrows in Figure 1(d)), creating a planar, interconnecting "nano-root" network, as clearly illustrated in the HIM image of Figure 1(d). Moreover, some of these interceptions deflect the growth fronts vertically away from the substrate base (e.g., marked by open squares in Figure 1(d)), lifting the GNIs up from the substrate while causing the GNIs to become more spherical. Away from the obstacles at the base, further growth in the vertical direction initiates the formation of the nanobelts with their characteristic rectangular cross sections, while some of the nanobelts undergo further deflection near the base before launching into more vertical growth (e.g., marked by open circles in Figures 1(d) and 1(e)). Further deposition results in an increase in the number and length of the nanobelts, leading to a dense mat of nanobelts. These nanobelts are found to have a characteristic rectangular cross section of 30 × 5 nm^2 to 70 × 30 nm^2 (Figure 1(f), inset), and they grow to 10–30 μm long after 90 min of deposition (Figure 1(f)). The GNIs appear to be settling on the wide side of the nanobelts at the tip. Furthermore, these nanobelts are straight and stiff with considerable rigidity and they grow to an extended length before notable bending occurs. It is of interest to note that the nanobelts with a bigger GNI catalyst and a smaller cross section are always found to be long, which is consistent with the VLS growth mechanism in which the higher SnO_2 vapour absorption rate provided by a larger catalyst surface on a smaller cross-sectional footprint would lead to a longer nanostructure.

The presence of an amorphous oxide layer over the entire ox-Si support of the GNI/ox-Si template, i.e., including the open area not covered by GNIs, prevents any potential crystalline correlation between the substrate and the growing SnO_2 nanobelts. However, as shown in our earlier work[20] and in Figure 1, the presence of this oxide layer is crucial to the detachment of GNIs and initiation of the VLS growth. In order to investigate the effect of substrate surface crystallinity on the SnO_2 nanostructure growth, we remove the oxide in the areas not covered by GNIs on the GNI/ox-Si template by a mild 2% HF etch for 12 min. At a deposition temperature of 500 °C, the H atoms on the resulted H-terminated Si areas are expected to undergo recombinative H_2 desorption,[27] leaving a pristine Si(100) surface. The final PLD-grown nanobelt morphology on this template is similar to that obtained on GNI/ox-Si template (supplementary information, Figures S1(a) and S1(b)),[28] while there are differences in the initial growth stages. Figure 2(a) and 2(b) show the HIM images of the nanobelts at the early stages of the PLD growth in 400 mTorr Ar at 500 °C on this HF-treated GNI/ox-Si template. Evidently, only a

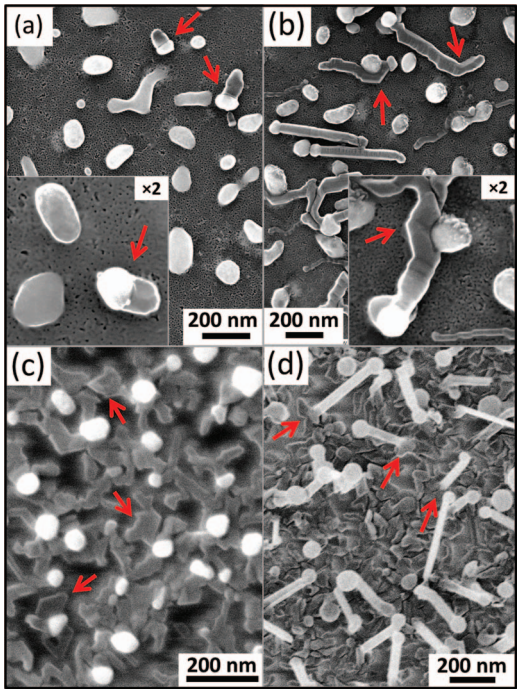

FIG. 2. HIM images of the nanobelts PLD-grown on a HF-etched GNI/ox-Si template at the (a) growth initiation stage, with the inset showing the differences between the active and inactive GNIs at a magnified view (active GNIs are marked with arrows), and (b) horizontal nanorod growth stage, with the inset depicting a vertical deflection and lift-off of GNI (horizontal kinks are marked by arrows), and on a GNI/Al_2O_3 template at the (c) planar nanostructure growth, and (d) lift-off and initiation of nanobelt growth stage.

small number of GNIs lead to SnO_2 nanostructure growth (Figure 2(a), marked by arrows) following the VLS growth mechanism, similar to that observed for the untreated GNI/ox-Si template (Figure 1(b)). Closer examination of the open area not covered by GNIs (Figure 2(a), inset) reveals a holey SnO_2 layer over the entire template, which also covers the GNIs not active in the VLS growth. This observation suggests that most of the GNIs are strongly attached to their neighbouring bare Si area at a sufficiently high deposition temperature of 500 °C, which prevents detachment of the GNIs and initiation of VLS growth. Continuing the laser ablation leads to further growth of the nanorods (Figure 2(b)), which with their increasing length become more likely to intercept other nanorods or GNIs on the surface. Kinks (marked by arrows in Figure 2(b)) appear to form with sharp turns of nearly 60° in the growth direction to avoid the GNIs and other nanorods, which suggests that the growing nanorods are highly crystalline and the kinks likely occur along their preferred crystalline directions. These interceptions could also deflect the nanorods upward, lifting off the GNIs and leading to the more vertical growth of the nanobelts (Figure 2(b), inset). After the GNI liftoff, short nanobelts with well-defined rectangular cross sections begin to emerge, and further deposition leads to increase in the lengths of the nanobelts with their uniform rectangular cross sections. Small SnO_2 nanocrystallites with irregular shapes (nanogravels) cover both the inactive GNIs and the open area of the active bare Si substrate not covered by GNIs (supplementary information, Figure S1(b), inset).[28] These nanogravels do not exhibit an appreciable change in size and appear to grow considerably slower than the nanobelts. This is likely due to a greater absorption rate of SnO_2 vapour on the GNIs than the adsorption rate on the rest of substrate leading to faster VLS growth of the nanobelts.

As shown in earlier studies, e.g., by Semancik and Cavicchi,[29] and confirmed in our own SnO_2 film deposition studies (results not shown), SnO_2 films are found to grow epitaxially in the (100) plane direction on the Al_2O_3(0001) surface. In order to investigate whether the presence of an oxide substrate with a good epitaxial relation to SnO_2 could affect the growth evolution and the crystalline growth direction of 1D SnO_2 nanostructures, we prepare SnO_2 nanobelts PLD-grown in 400 mTorr of Ar at 500 °C on a GNI/Al_2O_3(0001) template. Evidently, the HIM image in Figure 2(c) shows that the majority of the GNIs are lifted above the SnO_2 layer at the early stage of growth, which suggests that unlike the bare Si(100) and the ox-Si substrates, there appears to be little interaction between the GNI and the Al_2O_3 substrate. This difference between the Si and Al_2O_3 substrates has also led to the formation of bigger GNIs on Al_2O_3 compared to those on Si for a similar layer thickness of deposited gold. Deposition leads to the growth of irregularly shaped SnO_2 nanostructures planar to the surface in areas between the GNIs (e.g., marked by arrows in Figure 2(c)), indicative of the onset of a plausible epitaxial film growth. The presence of these nanostructures is found to restrict the VLS growth in the horizontal direction and promotes the early liftoff of GNIs (Figure 2(c)). Further deposition leads to initiation of the nanobelt growth on top of the as-formed planar nanostructures (e.g., marked by arrows in Figure 2(d)) with upward growth direction. As for the HF-etched GNI/ox-Si template, the final SnO_2 nanobelts obtained on the present GNI/Al_2O_3 template are found to have similar length and cross-sectional dimensions (supplementary information Figures S1(c)-S1(d)).[28] The epitaxial relation of the Al_2O_3(0001) surface with SnO_2 (to be supported by XRD data discussed below) has, therefore, restricted the horizontal growth of SnO_2 nanostructure before liftoff by the formation of planar structures in the early stage, without significantly affecting the final morphologies from that of the nanobelts obtained on the GNI/ox-Si or HF-etched GNI/ox-Si template. It should also be noted that the planar nanostructures eventually fill in the gaps between the GNIs and form a continuous layer on the Al_2O_3 substrate.

B. TEM studies of different growth stages

TEM studies are performed on the nanobelts PLD-grown in 400 mTorr Ar at 500 °C on the GNI/ox-Si, HF-etched GNI/ox-Si, and GNI/Al_2O_3 templates. The nanobelts grown on these three templates are found to exhibit similar crystallinity, with examples of typical features applicable to all three templates shown in Figures 3–5. Evidently, selected area electron diffraction (SAED) patterns in Figures 3(a) and 3(d) show the single-crystallinity of the nanobelts obtained on the GNI/ox-Si and HF-etched GNI/ox-Si templates, respectively. Furthermore, the growth axes (shown as arrows in the SAED patterns) are found to be either [101] (Figure 3(a)), or [010] (also equivalent to [100], Figure 3(d)), which correspond to the crystalline orientations shown schematically with the ball-and-stick unit-cell models of the tetragonal SnO_2 structure (Figures 3(a) and 3(d), insets). These orientations are also in excellent agreement with the observed atomic arrangements and spacings in their corresponding high-resolution TEM images (Figures 3(c) and 3(f)). The high-resolution TEM images taken across the width of the nanobelt near the edge and at the middle reveal near-perfect crystallinity (not shown), which is indicative of a very uniform and small belt thickness. Of the 15 different nanobelts examined by TEM in the present work, the nanobelts with the [101] growth direction are found to be generally short (1–5 μm in length), while the nanobelts with significantly longer lengths of 10–30 μm all have the [010] growth direction, as shown in the insets of low-resolution images (Figures 3(b) and 3(e) and supplementary information, Table S1).[28] Earlier studies on SnO_2 nanoribbons and nanowires grown by thermal evaporation,[21,30] however, have reported only the [101] growth direction. Our present observation of nanobelt growth with two different growth directions and growth rates, therefore, suggests different growth thermodynamics and kinetics for the catalyst-assisted PLD technique from the thermal evaporation methods. This difference can be attributed to two important factors affecting the growth process. The lower deposition temperature in this catalyst-assisted-PLD method compared to that of the thermal evaporation process leads to a lower thermal energy available for the atoms. The lower available energy could lead to entrapment of the atoms at various local free energy minima of the growth process, instead of the most energetically favorable minimum, leading to growth along various surface planes and directions. Another factor that is likely to affect the nanobelt

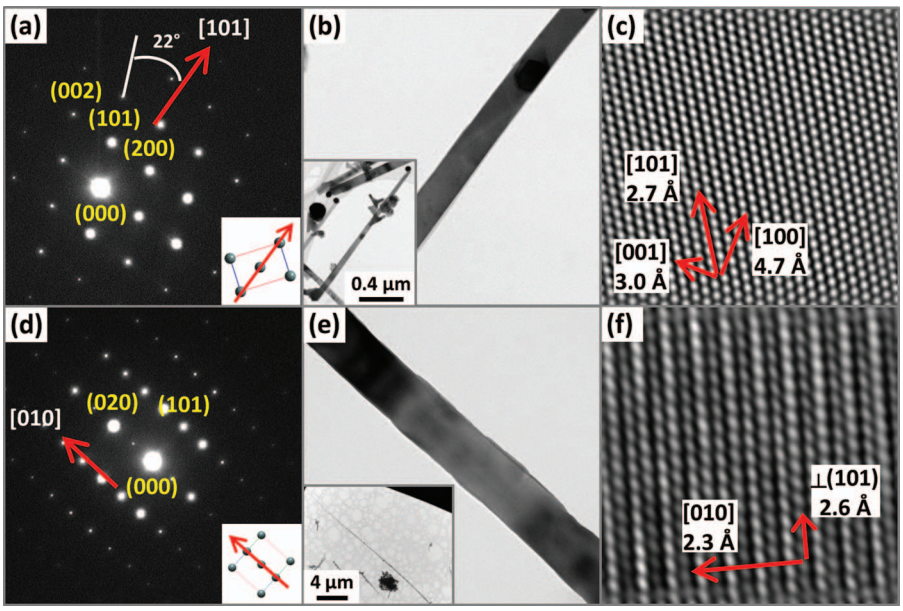

FIG. 3. (a) and (d) Selected-area electron diffraction (SAED) patterns, (b) and (e) low-resolution, and (c) and (f) high-resolution TEM images of nanobelts PLD-grown on (a)-(c) GNI/ox-Si and (d)-(f) HF-etched GNI/ox-Si templates. Ball-and-stick models for the SnO_2 unit cell [(a) and (d) insets] show the extracted crystal orientations, with the long arrows indicating the growth axes of the nanobelts. The low magnification images [(b) and (e) insets] illustrate the extended lengths of the nanobelts.

growth in the catalyst-assisted-PLD method is the presence of charged plasma species as building blocks of the nanostructure instead of neutral molecular or atomic gas species in the thermal evaporation method. This notable difference suggests that local electric fields can significantly alter the adsorption of species and the growth of nanobelts, which could induce drastic changes in the preferred growth orientation of the nanostructures. The well-resolved crystalline structures for the nanobelts (Figure 3(c)) further show that the nanobelts with the [101] growth axis have the (101) plane as their narrow-side surface and the (010) plane [also equivalent to (100)] as their wide-side surface, similar to what has been reported for the nanowires and nanoribbons grown by thermal evaporation.[21,30] The nanobelts with the [010] growth axis (Figure 3(f)) have the same (101) plane on their narrow sides, but their wide sides are perpendicular to the [−101]

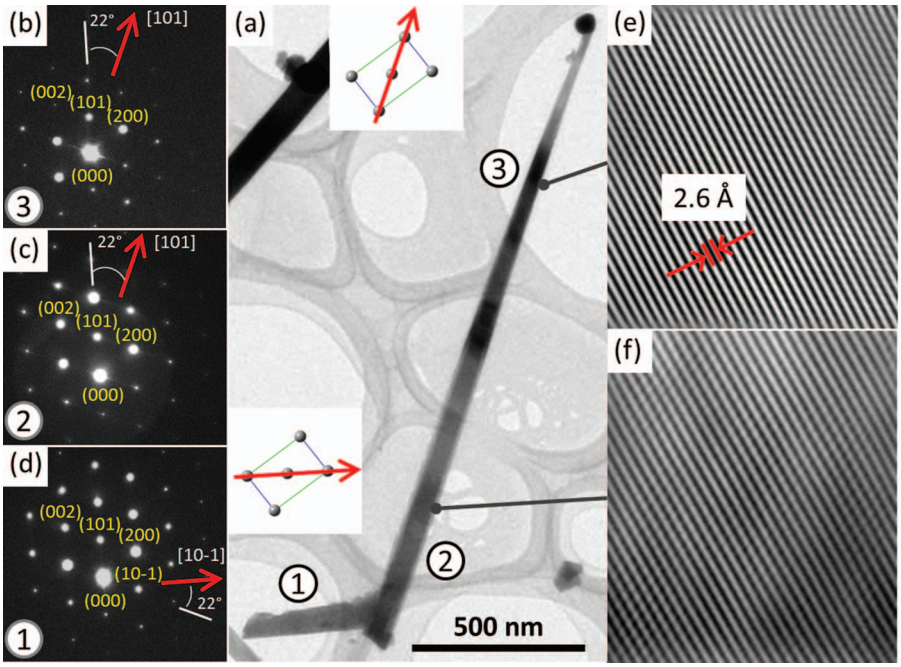

FIG. 4. (a) Low-resolution TEM image of a nanobelt with an initial nanorod growth followed by a change in the direction, and SAED patterns obtained at locations (b) 3, (c) 2, and (d) 1. High-resolution TEM images are also collected (e) and (f) at two points marked by lines on (a). The arrows in the ball-and-stick unit cell models and on SAED patterns show the growth axes of the nanobelt at their respective locations.

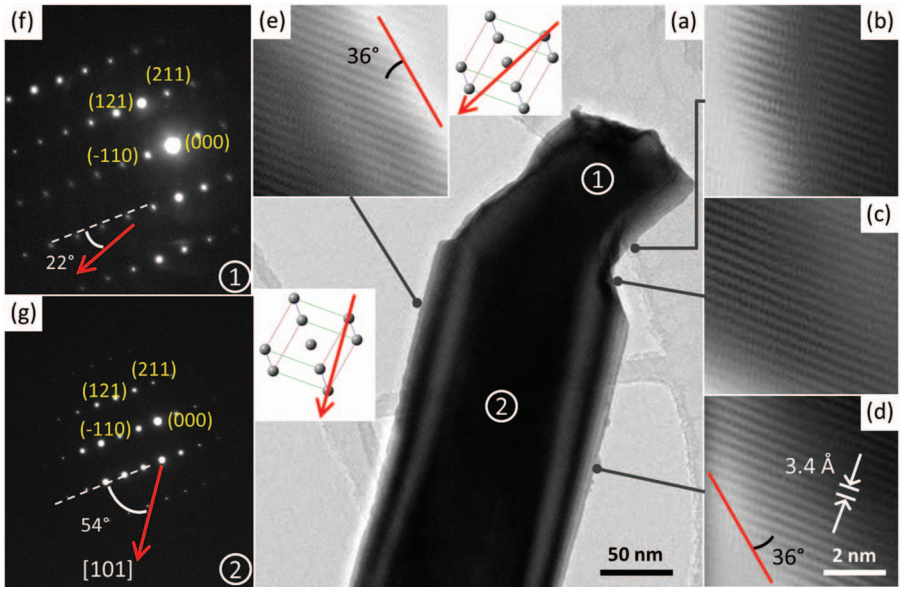

FIG. 5. (a) Low-resolution TEM image of a nanobelt with a kink near its base, and (b)-(e) high-resolution TEM images collected at selected locations marked by lines on (e), and (f) and (g) SAED patterns for locations 1 and 2, respectively. Arrows in the SAED patterns and the ball-and-stick unit cell models show the growth directions of the nanobelt at their respective locations.

(equivalent to [101]) direction and do not correspond to any crystalline plane. These latter crystalline growth orientations have not been observed in the thermal evaporation[16] and laser ablation studies.[14] The (201) plane, which makes a 87.3° angle with the [−101] direction, represents the closest plane for the wide side. Alternatively, the wide side could be considered as a (201) plane with a 2.7° miscut, which corresponds to a heavily stepped surface with high reactivity. Further investigations using surface science techniques including low-energy electron diffraction or scanning tunneling microscopy will be of great interest to elucidate the crystalline structure of this "stepped" surface.

In our surface morphology studies of the nanobelt growth (Figures 1 and 2), we observe that the nanobelts generally start to grow in a horizontal fashion until the growth front is deflected upward into a different direction by other objects on the substrate. Figure 4(a) shows an example of one such growth route of a nanobelt PLD-grown in 400 mTorr Ar at 500 °C on a GNI/Al_2O_3 template, in which a ∼400 nm long straight section is deflected, causing the growth to be redirected into the final ∼2 μm long straight section of the nanobelt. The SAED patterns collected before (Figure 4(d)) and after the deflection (Figure 4(c)) and near the Au tip (Figure 4(b)) reveal the same single-crystalline orientation at all three locations of the nanobelt, marked as 1, 2, and 3 in Figure 4(a). It should be noted that the zone axis is aligned at point 3 and the same alignment is used for other points to show the close crystalline orientation at different points on the nanobelt, in spite of the slight change in the alignment due to the existing taper along the length of the nanobelt. The growth axis before the deflection (marked by arrow in Figure 4(d)) is found to be along the [10–1] direction. The [10–1] direction is assigned based on the 22 ± 1° angle observed between the growth axis and the (10–1) diffraction direction (Figure 4(d)), and the corresponding atomic arrangement is illustrated in the ball-and-stick model (Figure 4(a), lower inset). After deflection by 113 ± 1°, the growth axis has evidently changed to the [101] direction (Figure 4(c)) and remains unchanged along the length of the nanobelt (Figure 4(b)). The high-resolution TEM images taken after the deflection (Figure 4(f)) and near the tip (Figure 4(e)) show well-resolved crystalline planes along the length of the nanobelt and parallel to the growth axis. Moreover, the interplane spacing is found to be 2.6 ± 0.1 Å for both locations, which corresponds to the lattice spacing of the (101) planes, in excellent accord with the SAED results.

Figure 5 shows the TEM results obtained near the base of a nanobelt PLD-grown in 400 mTorr Ar at 500 °C on a GNI/ox-Si template. Of particular interest is the kink observed in the low-resolution TEM image (Figure 5(a)), which shows a change in the growth direction at the initial growth stage of the nanobelt. The high-resolution images taken at different locations before (Figure 5(b)), at (Figure 5(c)), and after the kink at the edges of the nanobelts (Figures 5(d) and 5(e)) show well-resolved lattice planes all with the same spacing of 3.4 ± 0.1 Å, which corresponds to that of the (110) plane in bulk SnO_2 (PDF2#00-041-1445). Moreover, the lattice planes observed in all the high-resolution images have the same orientation, indicating a single-crystalline structure for the entire nanobelt in spite of the change in growth direction in the kink region. The SAED patterns (Figures 5(f) and 5(g)) taken before and after the change in the growth direction in the kink region (labeled as 1 and 2 in Figure 5(a)) also show a single-crystalline structure with the same crystalline orientation. The growth axis of the nanobelt before the kink (Figure 5(f)) makes a 22 ± 1° angle with the (−110) diffraction direction, which does not correspond to any low-index growth direction of the nanobelt, as depicted by the ball-and-stick model. This indicates a high index growth direction corresponding to a high-energy growth axis before the kink.

On the other hand, the growth axis after the kink makes a 54 ± 1° angle with the (–110) diffraction direction, which matches the [101] growth direction. This assignment is also in good agreement with the observed complementary 36 ± 1° angle of the (110) plane with respect to the [101] growth axis, as observed in the high-resolution TEM images in Figures 5(d) and 5(e).

These kinks are observed for some of the nanobelts (e.g., open circles in Figures 1(d) and 1(e)) right after the lift-off stage, suggesting that the growth along a high-index direction is caused by the spatial obstruction of the low-index growth direction by the obstacle that is causing the lift-off of the structure. Moreover, contact of the nanostructure with the obstacle is likely to change the surface energies of the planes at the contact point, especially with the noble metals (gold in this case, e.g., Figure 2(b), inset), which are known to show catalytic activities by modifying surface energies of the oxides. These factors are the likely cause of the high-energy growth direction. However, this growth is not thermodynamically stable when the growth front has progressed passed the obstacle, and the nanostructure then reverts back to an energetically favorable low-index growth front. This is in good accord with the observed short lengths, ~50–100 nm, of the kinks (which are only observed right after the lift-off stage) that are comparable to the obstacle size on the substrate.

The present TEM study, therefore, shows that the entire nanobelt has remarkably maintained its single-crystalline structure, despite the change in the growth direction during the growth evolution, from the initial horizontal growth on the substrate with various straight sections and deflections, to lift-off of the Au catalyst, and finally to nanobelt growth. If growth occurs along a low-index (i.e., low-energy) axis, the growth will continue along the same direction until obstruction is encountered (Figure 4). If, on the other hand, the growth direction happens to be disturbed to be not along a low-index axis, e.g., at the kink region in Figure 5, the growth will change back to a more energetically favorable low-index direction as soon as the growth front has passed the proximity of the cause of disturbance.

C. XRD studies of predominant growth directions

The crystalline structures of the SnO_2 films deposited on H–Si and ox-Si substrates, i.e., without the GNIs, and of the nanobelts PLD-grown on GNI/ox-Si, HF-etched GNI/ox-Si, and GNI/Al_2O_3 templates, all in 400 mTorr Ar at 500 °C are examined by GIXRD at an incidence angle of 0.3°. The GIXRD patterns observed for all the samples (Figure 6(a)) are in good agreement with the tetragonal phase of polycrystalline SnO_2 (PDF2#00-041-1445). In addition, two sets of peaks with weaker features corresponding to fcc Au (PDF2#00-004-0784) and to a gold–tin alloy that best matches the $Au_{17}Sn_3$ pattern (PDF2# 03-065-6388) are also observed for the nanobelt samples PLD-grown on supported GNI templates. In comparison with the reference pattern of polycrystalline SnO_2 (PDF2#00-041-1445), the SnO_2 films deposited on the bare H–Si and ox-Si substrates (i.e., without the GNIs) show higher relative intensities for the (101)

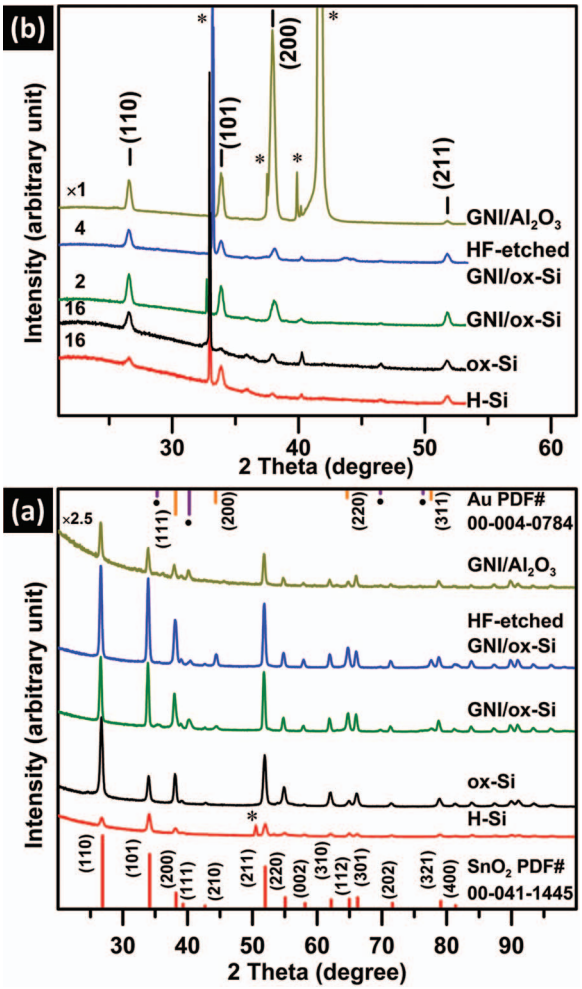

FIG. 6. (a) Glancing-incidence XRD patterns of the SnO_2 films and nanobelts measured at an incidence angle of 0.3°, compared with the reference patterns of fcc gold (PDF2#00-004-0784), and of tetragonal SnO_2 (PDF2#00-041-1445), along with the hexagonal $Au_{17}Sn_3$ alloy (PDF2#03-065-6388), marked by solid circles (•). (b) Symmetrical ω-2θ XRD patterns of the SnO_2 films and nanobelts. Asterisks (*) mark the peaks associated with the Si(100) in (a) and Al_2O_3(0001) substrates in (b).

and (110) peaks, respectively, indicating preferential growth in these respective planes. On the other hand, the nanobelts PLD-grown on GNI/ox-Si and HF-etched GNI/ox-Si exhibit discernibly higher relative intensities for both the (101) and (200) peaks, while the nanobelts PLD-grown on GNI/Al_2O_3 show a higher relative intensity only for the (200) peak [with the generally weaker signal due to the smaller substrate size (5×5 mm^2 for Al_2O_3 versus 10×10 mm^2 for ox-Si)]. The observed pattern for the gold-tin alloy further confirms the VLS growth mechanism of the nanobelts with dissolution of tin in the gold catalyst.

In order to investigate the crystal orientation of the growth with respect to that of the Si(100) or Al_2O_3(0001) substrate, we perform a symmetrical ω-2θ XRD study on the SnO_2 films and nanobelt samples after appropriate alignment with the respective substrate peak. The strong (101) and (110) peaks for the SnO_2 films grown, respectively, on the H–Si and ox-Si substrates (Figure 6(b)) indicate preferred growth in these respective planes. Because the ox-Si substrate is covered by an amorphous oxide layer, the observed

(110) preferred growth plane for the SnO_2 film could be attributed to the lower surface energy of the (110) plane in an Ar environment (i.e., an oxygen-deficient environment)[31] and/or a self-sputtering effect caused by energetic ions in the plasma. On the other hand, the observed (101) preferred growth plane for the SnO_2 film on the H-Si substrate suggests possible crystalline relations with the Si(100) substrate.

The nanobelts PLD-grown on the GNI-supported templates all exhibit generally more intense XRD features than the SnO_2 films on the ox-Si and H-Si substrates, in the order of HF-etched GNI/ox-Si < GNI/ox-Si < GNI/Al_2O_3 (Figure 6(b)). The increase in the intensities is consistent with the observed increased propensity for SnO_2 growth on the Al_2O_3 substrate and also with the increased number of active GNIs promoting VLS growth on these three supports (Figures 1 and 2). The latter leads to increased absorption of SnO_2 vapour and consequently an increase in the amount of deposited SnO_2. Furthermore, the XRD patterns for the nanobelts PLD-grown on GNI/ox-Si and on HF-etched GNI/ox-Si are found to be very similar to each other. Both nanobelt samples are considerably different from that for the SnO_2 films PLD-grown on ox-Si and H-Si, respectively. The observed intensity ratios for both (101)/(110) (=1.01) and (200)/(110) (=0.39) for the nanobelt sample grown on GNI/ox-Si template are considerably larger than the reference powder XRD pattern (0.75 and 0.21, respectively), which confirms the observed preferred growth planes of the nanobelts, as indicated in the GIXRD (Figure 6(a)) and TEM results (Figure 3). [The SnO_2(200) intensity has been obtained after due consideration of the close-lying Au(111) peak by fitting two peaks with FWHMs consistent with the other SnO_2 and Au peaks at 37.95° and 38.20°, respectively.] For the nanobelts grown on HF-etched GNI/ox-Si template, the expected growth plane of SnO_2 nanostructures grown in the open areas of the Si(100) substrate is (101), as observed for the SnO_2 film grown on H-Si (Figure 6(b)). The observed (101)/(110) intensity ratio (0.85), however, is notably smaller than that (1.01) observed for the nanobelts grown on the GNI/ox-Si template. Moreover, the (200)/(110) intensity ratio has dropped to the polycrystalline ratio level. The unexpected drop of the (101)/(110) intensity ratio and disappearance of the preferential (200) growth can be explained by considering pinning of the nanobelts with their (101) plane on the Si(100) substrate (as observed for SnO_2 growth on the H–Si substrate) at the horizontal growth stage. This pinning leads to the preferential growth of nanobelts in the [100] direction after the lift-off stage, as a result of the pinning in the (101) plane along with the observed single-crystallinity of the entire nanobelt (Figures 4 and 5). Growth of the nanobelts in the [100] direction with the (101) and (201) side surfaces would still give rise to an intense (101) peak, while the intensity of the (200) peak would drop, as is the case in this measurement. In contrast, growth in the [101] direction with the (101) and (200) side surfaces would have led to an increase in intensities of both (101) and (200) peaks, which is not the case. The extremely long nanobelts characteristic of growth in the (200) direction found on the HF-etched GNI/ox-Si also support this explanation (which is also in accord with our TEM results shown in Figure 3).

In marked contrast to the nanobelts grown on GNI/ox-Si and on HF-etched GNI/ox-Si templates, where the (101)/(110) intensity ratio is larger than the corresponding (200)/(110) ratio, the nanobelts grown on GNI/Al_2O_3 template exhibit the reverse trend (Figure 6(b)). The latter nanobelt sample shows a remarkably large (200)/(110) intensity ratio (6.48), due to the epitaxial relation of the (100) plane of SnO_2 with the Al_2O_3(0001) substrate, as observed in our film deposition studies (not shown) and as previously reported for the growth of SnO_2 thin films.[29] This larger (200)/(110) intensity ratio found for the nanobelts on the GNI/Al_2O_3 template can, therefore, be attributed to the planar SnO_2 nanostructures grown in the open areas not covered by GNIs on the Al_2O_3 substrate (Figure 2). Furthermore, a larger (101)/(110) intensity ratio (1.49) for the nanobelts grown on GNI/Al_2O_3, relative to the nanobelts grown on GNI/ox-Si (0.98), is also observed and can be attributed to the nanobelt growth with dominant (101) surfaces. It can, therefore, be concluded that the epitaxial relation of SnO_2 with the Al_2O_3(0001) surface leads to the spatial restriction of the nanobelts at the horizontal growth stage on the substrate caused by the formation of the planar epitaxial nanostructures in the open areas (Figure 2). The observed high intensity of the (101) peak can also be attributed to the restricted horizontal growth that causes the growth to continue in the pinned epitaxial growth direction. This pinning leads to the preferential growth of the nanobelts in the initial [100] direction with the (101) and (201) side surfaces, which gives rise to the observed intense (101) peak.

The presence of a crystalline relation between the SnO_2 films and the substrate can lead to a crystalline relation between the SnO_2 nanostructures and the substrate, which could therefore affect the [101] or [200] growth orientation of the nanobelts in different ways. This control of the growth direction generally occurs by pinning of the nanobelts in a specific crystalline orientation, the preferred growth direction observed for the growth of SnO_2 film on that substrate, in the initial growth stage on the substrate. This orientation pinning subsequently affects the final nanobelt growth direction because of the single-crystalline nature of the entire SnO_2 nanobelt throughout the growth including the initial growth stage.

IV. CONCLUSIONS

Growth evolution of the nanobelts deposited by a catalyst-assisted PLD method is investigated on three different templates using a mask-induced growth gradient technique. Various stages of the nanobelt growth on GNI/ox-Si templates are identified including the detachment of the Au catalyst (stage 1), horizontal growth on the substrate (stage 2), lift-off from the substrate due to spatial restriction on the substrate (stage 3), and the final upward nanobelt growth (stage 4). Nanobelt is found to preserve its single-crystallinity throughout the growth process, and we demonstrate that this can be used to promote the growth of the desired crystalline direction by pinning the nanobelts in the early horizontal growth stage to the appropriate substrate. This control on the growth axis can be either done through pinning with the

preferential growth direction on Si substrates, HF-etched GNI/ox-Si, or by pinning on substrates with epitaxial relation to SnO_2, GNI/Al_2O_3(0001). The present study, therefore, illustrates the growth evolution of the randomly oriented SnO_2 nanobelts for the first time, and shows how this information can be used to control the predominant crystalline growth orientation and consequently their side-surface planes. These different surface planes are expected to exhibit different surface selectivity, reactivity, and electronic properties. Manipulation of these surfaces along with the observed difference in the growth kinetics along different growth axes, as a differentiation criterion, will be of great importance to potential applications of these nanobelts as chemical sensors, (opto)transistors, and photonic components.

ACKNOWLEDGMENTS

The present work was supported by the Natural Sciences and Engineering Research Council of Canada.

[1]M. Law, D. J. Sirbuly, J. C. Johnson, J. Goldberger, R. J. Saykally, and P. Yang, Science **305**, 1269–1273 (2004).
[2]M. S. Arnold, P. Avouris, Z. W. Pan, and Z. L. Wang, J. Phys. Chem. B **107**, 659–663 (2003).
[3]Z. Liu, D. Zhang, S. Han, C. Li, T. Tang, W. Jin, X. Liu, B. Lei, and C. Zhou, Adv. Mater. **15**, 1754–1757 (2003).
[4]X. D. Bai, P. X. Gao, Z. L. Wang, and E. G. Wang, Appl. Phys. Lett. **82**, 4806 (2003).
[5]Z. L. Wang and J. Song, Science **312**, 242–246 (2006).
[6]H. Huang, Y. C. Lee, O. K. Tan, W. Zhou, N. Peng, and Q. Zhang, Nanotechnology **20**, 115501 (2009).
[7]R. G. Gordon, MRS Bull. **25**, 52–57 (2000).
[8]R. Dolbec and M. A. El Khakani, Appl. Phys. Lett. **90**, 173114 (2007).
[9]Y. Cheng, P. Xiong, C. S. Yun, G. F. Strouse, J. P. Zheng, R. S. Yang, and Z. L. Wang, Nano Lett. **8**, 4179–4184 (2008).
[10]J. H. He, T. H. Wu, C. Hsin, K. M. Li, L. J. Chen, Y. L. Chueh, L. J. Chou, and Z. L. Wang, Small **2**, 116–120 (2006).
[11]H. Huang, O. K. Tan, Y. C. Lee, M. S. Tse, J. Guo, and T. White, Nanotechnology **17**, 3668–3672 (2006).
[12]F. Gu, S. Wang, H. Cao, and C. Li, Nanotechnology **19**, 095708 (2008).
[13]L. Qin, J. Xu, X. Dong, Q. Pan, Z. Cheng, Q. Xiang, and F. Li, Nanotechnology **19**, 185705 (2008).
[14]J. Q. Hu, Y. Bando, Q. L. Liu, and D. Golberg, Adv. Funct. Mater. **13**, 493–496 (2003).
[15]F. Paraguay-Delgado, W. Antúnez-Flores, M. Miki-Yoshida, A. Aguilar-Elguezabal, P. Santiago, R. Diaz, and J. A. Ascencio, Nanotechnology **16**, 688–694 (2005).
[16]Z. R. Dai, J. L. Gole, J. D. Stout, and Z. L. Wang, J. Phys. Chem. B **106**, 1274–1279 (2002).
[17]L. C. Tien, S. J. Pearton, D. P. Norton, and F. Ren, Appl. Phys. A **91**, 29–32 (2008).
[18]C. Czekalla, J. Guinard, C. Hanisch, B. Q. Cao, E. M. Kaidashev, N. Boukos, A. Travlos, J. Renard, B. Gayral, D. Le Si Dang, M. Lorenz, and M. Grundmann, Nanotechnology **19**, 115202 (2008).
[19]M. Lorenz, E. M. Kaidashev, A. Rahm, T. Nobis, J. Lenzner, G. Wagner, D. Spemann, H. Hochmuth, and M. Grundmann, Appl. Phys. Lett. **86**, 143113 (2005).
[20]S. Bazargan and K. T. Leung, J. Phys. Chem. C **116**, 5427–5434 (2012).
[21]Z. R. Dai, Z. W. Pan, and Z. L. Wang, Solid State Commun. **118**, 351–354 (2001).
[22]Y. Wu, Y. Cui, L. Huynh, C. J. Barrelet, D. C. Bell, and C. M. Lieber, Nano Lett. **4**, 433–436 (2004).
[23]V. Schmidt, S. Senz, and U. Gösele, Nano Lett. **5**, 931–935 (2005).
[24]W. Kern, *Handbook of Semiconductor Wafer Cleaning Technology* (William Andrew, Norwich, NY, 1993).
[25]Y. Sohn, D. Pradhan, A. Radi, and K. T. Leung, Langmuir **25**, 9557–9563 (2009).
[26]R. S. Wagner and W. C. Ellis, Appl. Phys. Lett. **4**, 89–90 (1964).
[27]J. J. Boland, Phys. Rev. Lett. **67**, 1539–1542 (1991).
[28]See supplementary material at http://dx.doi.org/10.1063/1.4794741 for growth axis dependent length distribution and late stage nanobelt growth morphology on HF-etched GNI/Ox-Si and GNI/Al_2O_3 templates.
[29]S. Semancik and R. Cavicchi, Thin Solid Films **206**, 81–87 (1991).
[30]Z. W. Pan, Z. R. Dai, and Z. L. Wang, Science **291**, 1947–1949 (2001).
[31]M. Batzill and U. Diebold, Prog. Surf. Sci. **79**, 47–154 (2005).